Modelling the crush behaviour of thermoplastic composites

Modelling the crush behaviour of thermoplastic composites

Wei Tan[a,b], Brian G. Falzon[b,*]

[a] School of Mechanical and Electrical Engineering, Central South University, Changsha, 410083, China

[b] School of Mechanical and Aerospace Engineering, Queen's University Belfast, Belfast, BT9 5AH, UK

* Corresponding author: b.falzon@qub.ac.uk (B.G. Falzon)

Tel: +44 (0)28 9097 5640

Abstract

Thermoplastic composites are likely to emerge as the preferred solution for meeting the high-volume production demands of passenger road vehicles. Substantial effort is currently being directed towards the development of new modelling techniques to reduce the extent of costly and time consuming physical testing. Developing a high-fidelity numerical model to predict the crush behaviour of composite laminates is dependent on the accurate measurement of material properties as well as a thorough understanding of damage mechanisms associated with crush events. This paper details the manufacture, testing and modelling of self-supporting corrugated-shaped thermoplastic composite specimens for crashworthiness assessment. These specimens demonstrated a 57.3% higher specific energy absorption compared to identical specimen made from thermoset composites. The corresponding damage mechanisms were investigated *in-situ* using digital microscopy and post analysed using Scanning Electron Microscopy (SEM). Splaying and fragmentation modes were the

primary failure modes involving fibre breakage, matrix cracking and delamination. A mesoscale composite damage model, with new non-linear shear constitutive laws, which combines a range of novel techniques to accurately capture the material response under crushing, is presented. The force-displacement curves, damage parameter maps and dissipated energy, obtained from the numerical analysis, are shown to be in a good qualitative and quantitative agreement with experimental results. The proposed approach could significantly reduce the extent of physical testing required in the development of crashworthy structures.

Keywords: A. Polymer-matrix composites (PMCs); B. Fracture; C. Finite element analysis; Crashworthiness

1. Introduction

Thermoplastic resins offer a number of advantages over conventional thermosetting resins such as epoxies, particularly in exhibiting excellent performance in impact resistance and energy absorption [1]. While thermoset composites have dominated the aerospace industry, thermoplastics composites are likely to emerge as the preferred solution for meeting the high-volume production demands of passenger road vehicles [1, 2].

Corrugated webs manufactured with carbon fibre (CF)/Epoxy have been used for several energy-absorbing applications in helicopter sub-floor [3] and aircraft fuselage structures [4]. Moreover, the self-supporting nature of derived corrugated test specimens removes the need for a test fixture for crush testing, which could also influence the crush behaviour of the specimen [5, 6]. Not only do such structures display greater stability under loading, but they are also relatively easy to manufacture, compared to tubular specimens, using compression moulding, thermoforming or injection moulding techniques. The high fracture toughness associated with thermoplastic

composites implies that they have great potential in improving the crashworthiness performance of composite automotive structures.

The complex interacting failure modes, associated with carbon fibre composite material under dynamic impact, present numerous challenges in predicting the crashworthiness of composite structures. Current assessment of composite structures, under crush loading, relies on extensive, costly and time-consuming experimental testing [7, 10]. It is therefore desirable to develop a cost-effective computational approach to predict the response of composite structures, during crushing, to minimize the physical testing of components. Many researchers have made efforts to improve the accuracy of numerical models for simulating composite crushing, using commercially available models. A shell-based formulation (Mat54) in LS-DYNA, for arbitrary orthotropic materials, was employed by Feraboli et al [7]. A mesoscale model with layered shell elements combined with a numerical trigger was used to simulate the response of self-supporting carbon-epoxy hat-shaped crush elements with the software package PAM-CRASH by David and Johnson [8, 9]. A plug-in tool for ABAQUS/Explicit, CZone, which is dependent on empirical coupon and component data to generate input parameters for the computational model, was employed to simulate the crushing of large scale structures [10]. These commercially available models have been developed to use plane stress shell elements, which assume that through thickness stresses are negligible. This assumption cannot be made for structures being crushed as the loading on a typical section of material in a crushing structure is highly complex and three-dimensional.

Physically-based approaches, quantitatively accounting for the progression of the actual damage mechanisms, have also been developed to model crush behaviour. Pinho et al. [11], Palanivelu et al. [12] and Fleming [13] proposed various numerical models for the crushing simulation of fibre-reinforced composite materials. Sokolinsky et al.[14] investigated a corrugated carbon-epoxy fabric composite plate subjected to quasi-static crushing, where intralaminar failure was simulated

using an in-plane constitutive model and delamination was modelled by cohesive surface contact. Israr et al. [26] presented a pseudo-2D finite element model for mixed-mode crushing of laminated plates by introducing a free-face-crushing concept to represent localized crushing, similar to a strain-based element deletion criterion. However, the interactive damage mechanisms and material non-linearity with degraded shear modulus are not handled well by these models. Due to the failure of neighbouring material, unloading and reloading is expected in the local region of composite structures under crushing, which is not captured by some of these models. The contribution of different damage mechanisms to the overall energy absorption during crushing have not been presented in the literature either.

A composites damage model based on fracture and continuum damage mechanics, has been developed by Falzon's research group, initially for predicting low-velocity impact damage [15-17] and compression-after-impact strength [18] and was subsequently used to capture crushing behaviour, validated using experimental data from wedge-shape specimens [19]. This computational model assumed that the shear modulus remained constant under shear loading.

In this paper, the sample preparation and experimental testing of thermoplastic corrugated composite specimens are described first, followed by a detailed investigation of the crushing damage mechanisms. This is followed by a brief overview of the new composite damage model. The proposed model delivers a significant improvement in non-linear shear behaviour, by accounting for modulus degradation, load reversal and mixed-mode intralaminar damage progression. The measured intrinsic ply-level material properties in [20] were used as input parameters for the finite element analysis to validate the model against experimental results. This work also presents a thorough understanding of damage and energy absorbing mechanisms during the crushing of corrugated-shaped composite structures.

2. Materials and Methods

2.1 Materials and sample preparation

The fibre reinforced composite material used in this study is unidirectional carbon fibre (AS4D 12K) / poly-ether-ketone-ketone (PEKK) pre-preg tape provided by Cytec Engineered Materials® (part of the Solvay Group). Cross-ply $[0/90]_{3s}$ corrugated samples were fabricated with a Collin® heated press in a consolidation cycle following the manufacturer's specifications. A steel mould was designed to form the panels from which the test specimens where produced, as shown in Fig.1. A thin polyimide film (12.7μm thick), coated with release agent, was used on each tool surface in contact with the corrugated panels to facilitate the demoulding process.

After curing, one edge of each composite panel was chamfered at 45° and cut into two specimen types with slightly different geometries. One specimen type had a corrugated trapezoidal, or 'hat' cross section with three segments, or 'half –waves', and referred to as a 'Hat-3p' specimen. The other specimen type had semi-circular corrugations and referred to as a 'Semi-3p' specimen. These specimens are shown in Figure 2a where it is noted that each have extended unloaded edges for additional stability. The non-chamfered loaded edge of each specimen was polished and inspected by optical microscopy (Figs. 2b and 2c). A high quality lay-up was achieved with no evidence of fibre waviness or wrinkling. Fig. 3a shows the 0° fibre orientation on the specimens and Fig. 3b show the cross section dimensions.

2.2 Test method

The specimens were tested in compression between two flat steel platens in a Hounsfield machine with a 50kN load cell. The load response was recorded directly from the load cell while the displacement was obtained from the instrumented moving crosshead. The crosshead speed was set at 5mm/min, giving a nominal strain rate of $1 \times 10^{-3}/s$. The out-of-plane displacement was

monitored by Digital Image Correlation (DIC). The gauge section at the centre of the specimen was sprayed white, followed by a black speckle to facilitate DIC measurements. The failure process in the crushing zone was recorded with two digital microscopes shown in Fig. 4.

2.3 Crashworthiness metrics

The performance of crashworthy composite structures can be evaluated by their total energy absorption (E_s), specific energy absorption (SEA), peak force (F_P), steady-state force (F_{SS}) and crush efficiency (CE). The total energy absorption, E_s , is the area under the force (F) –displacement (S) curve. SEA is defined as the energy absorbed per unit mass of material, $SEA = \int FdS/m$, which is a critical assessment of performance for lightweight structures used in aircraft or road vehicles. F_P is the highest force experienced during the crush event and has a direct correlation with the extent of potential injury to passengers. F_{SS} is the mean force during steady-state crushing of the specimen and is a good indicator of the energy absorption capability of crashworthy structures. Crush efficiency, CE, is the ratio between F_{SS} and F_P indicating the nature of the crush response. A high-energy absorbing crashworthy structure is one which undergoes progressive failure where the peak force is not appreciably higher than the steady-state force, i.e. one with high crush efficiency.

3. Failure mechanisms

3.1 Typical damage modes

Understanding the overall crushing damage mechanisms is crucial for improving the crashworthiness performance of automotive structures as well as providing a reliable validation for the numerical models. Damage at the mesoscale may be described with reference to the axial and circumferential directions. Damage mechanisms in the axial direction can be generally categorised by two primary failure modes – a splaying mode and a fragmentation mode, as shown in Fig. 5. In the splaying mode, bending leads to the formation of continuous fronds. Some 0˚ plies fail due to longitudinal fibre

fracture, which may further involve fibre pull-out, while most 90˚ plies fail due to transverse splitting and matrix cracking. Extensive mixed-mode interlaminar delamination will also be evident. Mode I dominant delamination is often exacerbated by debris acting like a 'wedge' in further driving delamination. Compressive loading also leads to fibres fragmentation of 0˚ plies at the contact surface and localized damage of 90˚ plies due to matrix crushing and multiple shear cracks at the tip of the plies. The final intralaminar ply failure consists of fibre breakage and matrix cracking due to the combination of bending, compression and shear. Similar observations have also been presented by Isar et al.[21], Tan et al. [19] and Grauers et al. [22].

The complex crushing damage mechanisms of the tested corrugated structures, in the circumferential direction, are described in Fig. 6a. These are consistent with the findings by Palanivelu et al. [23] and Chiu et al. [24]. In the 0˚ plies, the main forms of failure are ply splitting and brittle fibre fracture via bending or shearing. Failure in the 90˚ plies was predominantly shear-induced matrix cracking, triggered by compressive loading transverse to the ply. Fibre tensile and compressive splits can be seen in Fig. 6b at both sides of the corrugation, when the fronds are forced to move outwards and inwards respectively (red arrows indicate the trends). Although the splits occur extensively during crushing, the adjacent plies formed continuous fronds.

3.2 Fractographic analysis

The fracture surface was examined using Scanning Electron Microscopy (SEM) at several locations to investigate microscale damage as shown in Fig. 7. The crushed surface in Fig. 7a indicates matrix crushing and extensive fibre fracture. This SEM image was taken from a continuous frond. The crushed matrix was generated when splaying fronds experienced friction with the metallic base plate. The sliding of the frond doesn't affect the overall load response (vertical reaction force), which is mainly controlled by the vertically-aligned laminates. The friction between the frond and plate may influence the delamination of the outer plies of the laminates. Fig. 7b shows the failure due to

shearing. Fig. 7c demonstrates the fracture of fibres (Fig. 6c-SEM①) at three locations, the 0˚ ply tensile failure can be seen in ①-A and ①-B and the 90˚ ply tensile failure is shown in ①-C. Fig. 7d shows a set of SEM images of the inward damaged fragment (Fig. 6c-SEM②), where 0˚ ply bending failure and 90˚ ply compressive failure are indicated in ②-A and ②-B. ②-A shows evidence of fibre pull-out at the bending –induced fracture surface.②-C shows that fibres were mainly fractured due to bending.

4. Finite element model

4.1 Intralaminar damage model

The developed intralaminar damage model is based on a continuum damage mechanics approach proposed by Lemaitre and Chaboche [25] , as a method to determine the behaviour of a material under damage-inducing loads. The effective stresses are defined as stresses transmitted across the intact part of the cross-section in a Representative Volume Element (RVE). The components of the effective stress tensor, $\tilde{\sigma}$, and true stress tensor, σ , can be linked by the damage tensor, $\mathbf{D}$, undamaged material elasticity tensor $\mathbf{C}$ and the strain tensor ε, $\sigma = \mathbf{D}\tilde{\sigma}$ and $\tilde{\sigma} = \mathbf{C}\varepsilon$. The stress-strain relationship under the longitudinal tension/compression or transverse tension is elastic, while under transverse compression or shear loading the material exhibits plasticity and non-linear behaviour. Therefore, an accurate description of non-linear shear behaviour is required. Base on the damage model presented in [15-19], the failure criteria and damage model is briefly described below, incorporating the new non-linear shear model.

4.1.1 New non-linear shear behaviour

There are many models dealing with non-linear shear behaviour available in the literature. Van Paepegem et al. [26, 27] proposed a phenomenological model which introduced shear damage and permanent shear strain as two state variables to model the non-linear shear behaviour. Vogler [28]

and Camanho [29] presented a fully three-dimensional transversely isotropic elastic–plastic constitutive model for composite materials to represent the plasticity-based non-linearities under multiaxial loading conditions. Vyas et al [30] presented a plasticity-based approach to model the nonlinear mechanical response of polymer–matrix fibre-reinforced composites with unidirectional plies under quasi-static loading. However, the interactive damage mechanisms and material non-linearity with degraded shear moduli are not handled well by these models. Loads that induce damage may also cause local unloading, which is not captured by these models. It is therefore essential to continue the work in the understanding and simulation of composite structures under shear loading to address current limitations. A new composite non-linear damage model that accounts for inelastic deformation, stiffness degradation and load reversal is presented. Prior to damage initiation, shear loading and unloading occurs along gradients defined by the initial shear modulus, G_{ij}^{ini}, and degraded shear modulus, G_{ij}^{*}, shown in Fig. 8a. According to plastic-damage theories, the plastic strain represents all irreversible deformations including those caused by microcracks. The shear strain, γ_{ij}, was decomposed into the elastic part, $\gamma_{ij,el}$, and the plastic part, $\gamma_{ij,in}$,

$$\gamma_{ij} = \gamma_{ij,el} + \gamma_{ij,in} \qquad i \neq j = 1,2,3. \tag{1}$$

The elastic strain is given by,

$$\gamma_{ij,el} = \tau_{ij}/G_{ij}^{*} \ . \tag{2}$$

Since the in-plane and out-of-plane behaviour do not differ significantly under shear loading and due to the lack of experimental results for out-of-plane shear behaviour, similar curves have been used to model out-of-plane shear non-linearities. The in-plane and out-of-plane stress-strain constitutive laws are modelled using an exponential model,

$$\tau_{ij}(\gamma_{ij}) = \begin{cases} \tau_{ij}^{Y}\left[exp(\alpha\gamma_{ij}) - exp(\beta\gamma_{ij})\right], & \gamma_{ij} \geq 0 \\ \tau_{ij}^{Y}\left[-exp(-\alpha\gamma_{ij}) + exp(-\beta\gamma_{ij})\right], & \gamma_{ij} < 0 \end{cases}, \quad (3)$$

where τ_{ij}^{Y} is the initial yield strength, determined by translating the shear chord modulus of elasticity along the strain axis from the origin to 2% strain. α is a strain hardening coefficient and β controls the initial shear modulus and elastic-plastic transition region .To characterize the degradation of the shear modulus, defined as the secant shear modulus for one loading-unloading cycle, a degraded shear modulus $G_{ij}^{*,t+\Delta t}$ was introduced and fitted according to the strain-degraded modulus curve in Fig. 8. The degraded modulus was coupled with the plastic deformation in the constitutive relation, making it convenient to obtain the fitting parameters from experiment results,

$$G_{ij}^{*,t+\Delta t} = p_1 exp(p_2\left|\gamma_{ij}^{t+\Delta t}\right|) + p_3 exp(p_4\left|\gamma_{ij}^{t+\Delta t}\right|), \quad (4)$$

where $p_i(i = 1,2,3,4)$ are the coefficients for the degraded modulus and Δt is the time increment. An isotropic hardening rule, based on the elastic predictor method, was used to determine the undamaged response, illustrated in Fig. 8b, showing the steps involved in determining the final load state. The elastic stress predictor is given by $\tau_{ij,el}^{t+\Delta t} = \tau_{ij,el}^{t} + G_{ij}^{*,t}\Delta\gamma_{ij}$. An initial stress state $(\gamma_{ij}^{t}, \tau_{ij}^{t})$ is reached after partial unloading along the *in-situ* shear modulus (G_{ij}^{*}). The stress state after subsequent reloading to $\gamma_{ij}^{t+\Delta t}$ depends on whether plastic yielding has occured. Initially, the stress is assumed to increase elastically to $\tau_{ij,el}^{t+\Delta t}$. Yielding occurs when $\tau_{ij,el}^{t+\Delta t} > \tau_{ij}(\gamma_{ij}^{t+\Delta t})$, which results in the increased inelastic strain of $\gamma_{ij,in}^{t+\Delta t}$ and reduced effective stress of $\tau_{ij,E}^{t+\Delta t} = \tau_{ij}(\gamma_{ij}^{t+\Delta t})$. Alternatively, if $\tau_{ij,el}^{t+\Delta t} < \tau_{ij}(\gamma_{ij}^{t+\Delta t})$, yielding has not occurred so the inelastic strain remains constant and $\tau_{ij,el}^{t+\Delta t}$ is retained as the final stress state. For a material under a reversed loading condition, the subsequent yield stress is determined by the isotopic hardening approach, which assumes the reversed compressive/shear yield stress is equal to the tensile/original yield

stress. Isotropic hardening only applies while the loading remains below the threshold of matrix damage initiation. Once matrix cracking initiates, unloading occurs along the reduced secant shear modulus to the permanent plastic strain $\gamma_{ij,in}^{o}$ at damage initiation.

4.1.2 Brief overview of failure initiation criteria

A strain-based damage initiation function was used for simplicity to model the material response in the longitudinal direction. The failure initiation criterion based on Puck and Schürmann's [31] and Catalanotti et al. [32] was used for predicting matrix damage behaviour. A brief summary of fibre-dominated and matrix-dominated failure criteria are given below. Full details of the criteria may be found in [18, 19] and are not repeated here for brevity.

Fibre-dominated

$$\varepsilon_{11} > 0,\ F_{11}^{T}(\varepsilon_{11}) = \left(\frac{\varepsilon_{11}}{\varepsilon_{11}^{OT}}\right)^2 \geq 1 \tag{5}$$

$$\varepsilon_{11} < 0,\ F_{11}^{C}(\varepsilon_{11}) = \left(\frac{\varepsilon_{11}}{\varepsilon_{11}^{OC}}\right)^2 \geq 1 \tag{6}$$

Matrix-dominated

$$\sigma_{NN} \leq 0,\ F(\theta) = \left(\frac{\sigma_{LN}}{S_{12} - \mu_{LN}\,\sigma_{NN}}\right)^2 + \left(\frac{\sigma_{NT}}{S_{23} - \mu_{NT}\,\sigma_{NN}}\right)^2 \tag{7}$$

$$\sigma_{NN} > 0,\ F(\theta) = \left(\frac{\sigma_{NN}}{S_{23}}\right)^2 + \left(\frac{\sigma_{LN}}{S_{12}}\right)^2 + \left(\frac{\sigma_{NT}}{S_{23}}\right)^2 + \lambda\left(\frac{\sigma_{NN}}{S_{23}}\right)\left(\frac{\sigma_{LN}}{S_{12}}\right)^2 + \kappa\left(\frac{\sigma_{NN}}{S_{23}}\right) \tag{8}$$

Where F_{11}^{T} and F_{11}^{C} are the failure indices for tensile and compressive loading, and the failure initiation strains (ε_{11}^{OT} and ε_{11}^{OC} for tension and compression, respectively) were determined by the strengths in the respective directions, i.e. $\varepsilon_{11}^{OT} = X^T/E_{11}^{0}$ etc. The stress tensor $\sigma_{LNT} = \left[T\left(\theta_f\right)\right]\sigma_{123}[T\left(\theta_f\right)]^T$ on the fracture plane was rotated using the standard transformation matrix $T\left(\theta_f\right)$, from the material coordinate system (123) rotated to the fracture plane coordinate system (LNT), where θ_f is defined as the angle of potential fracture plane.. Parameters κ and λ are

given by $\kappa = S_{23}^2 - (Y_T)^2/S_{23}Y_T$, $\lambda = 2\mu_{LN}S_{23}/S_{12} - \kappa$, S_{12} and S_{23} are the shear strengths.The transverse friction coefficients μ_{NT} and μ_{LN}, defined in [13], are based on Mohr-Coulomb theory where $\mu_{NT} = -1/\tan(2\theta_f)$, $S_{23} = Y_C/2\tan(\theta_f)$ and $\mu_{LN} = \mu_{NT}S_{12}/S_{23}$, Y_C and Y^T are the transverse compressive strength and transverse tensile strength. The fracture plane orientation, θ_f, is typically found to be approximately 53° for unidirectional composites [13] under uniaxial transverse compressive loading. For a general 3D load state, the orientation is not known *a priori* and is determined by the angle which maximizes the matrix dominated failure criteria functions. Brent's algorithm [33] was used for this purpose which combines a golden section search with parabolic interpolation.

4.1.3 Damage evolution

The damage tensor is a function of three monotonically increasing damage variables, bound by 0 (no damage) and 1 (complete failure), each one relating to a form of damage mode under a different loading state. d_{11}^T refers to tensile damage in the fibre direction, d_{11}^C refers to compressive damage in the fibre direction and d_{mat} refers to matrix cracking due to a combination of transverse tension/compression and shear loading. The damage parameter associated with loading in the longitudinal direction is given by,

$$d_{11}^{T(C)}(\varepsilon_{11}) = \frac{\varepsilon_{11}^{FT(C)}}{\varepsilon_{11}^{FT(C)} - \varepsilon_{11}^{OT(C)}}\left(1 - \frac{\varepsilon_{11}^{OT(C)}}{\varepsilon_{11}^{T(C)}}\right), \tag{9}$$

where the failure strains, $\varepsilon_{11}^{FT(C)}$, at which net-section fracture across the element occurs, is determined by the critical energy release rates $\Gamma_{11}^{T(C)}$, and longitudinal tensile/compressive strength $X_{T(C)}$, given by,

$$\varepsilon_{11}^{FT(C)} = 2\Gamma_{11}^{T(C)}/X_{T(C)}\, l_{fib}, \tag{10}$$

where l_{fib} is the characteristic length. Mesh objectivity of the model was achieved by employing the crack-band model of Bažant and Oh [13].The characteristic length associated with the longitudinal direction is determined by $l_{fib} = V/A$, where V is the element volume and the fracture surface area, A, is calculated using an approach proposed in [18].

The non-linear shear behaviour and damage propagation is shown in Fig. 9. To quantify the modulus degradation during the strain hardening part and damage evolution in the strain softening part, two parameters are introduced to describe the damage propagation under transverse compression and shear loading: (i) shear damage in the strain hardening part, d_{ij}^{I}, and (ii) shear damage in the strain softening part, d_{ij}^{II};

$$d_{mat} = \begin{cases} d_{ij}^{I} & \gamma_{ij} < \gamma_{ij}^{o} \\ d_{ij}^{II} & \gamma_{ij} > \gamma_{ij}^{o} \end{cases} \tag{11}$$

$$d_{ij}^{I} = 1 - G_{ij}^{*}/G_{ij}^{ini}, \tag{12}$$

$$d_{ij}^{II} = d_{ij}^{I} + \left(1 - d_{ij}^{I}\right)\frac{\gamma_{ij}^{f} - \gamma_{ij,in}^{o}}{\gamma_{ij}^{f} - \gamma_{ij}^{o}}\left(\frac{\gamma_{ij} - \gamma_{ij}^{o}}{\gamma_{ij} - \gamma_{ij,in}^{o}}\right), \tag{13}$$

where the final failure strain, γ_{ij}^{f}, is determined by $\gamma_{ij}^{f} = 2\mathrm{g}_{ij}/\tau_{ij}^{o} + \gamma_{ij,in}^{o}$ and $\mathrm{g}_{ij} = \Gamma_{ij}/l_{mat}$. $\gamma_{ij,in}^{o}$ is the plastic strain at the onset of failure, l_{mat} the characteristic crack length described in [18] and τ_{ij}^{o} is the shear strength. g_{ij} is the volume energy release rate associated with the elastic fracture energy (shaded red part in Fig. 8a) and Γ_{ij} is the shear fracture toughness. A quadratic interpolation function was used for the mixed-mode fracture energy [18].

4.2 Interlaminar damage model

The surface-based cohesive behaviour in ABAQUS/Explicit [34] was used to capture delamination using a bilinear traction-separation relationship. This approach is a convenient means to model the cohesive connections without the need to define cohesive elements and tie constraints. Contact

separations are the relative displacements between the nodes on the slave surface and their corresponding projection points on the master surface along the contact normal and shear directions. Traction stresses are defined as the cohesive forces acting along the contact normal and shear directions divided by the current area at each contact point. Failure initiation was governed by a quadratic stress criterion,

$$\left(\frac{t_1}{t_1^0}\right)^2 + \left(\frac{t_2}{t_2^0}\right)^2 + \left(\frac{\langle t_3 \rangle}{t_3^0}\right)^2 \leq 1, \tag{14}$$

where $t_i (i = 1,2,3)$ are the traction stress vectors in the in-plane (1,2) and normal (3) directions, respectively, and t_i^0 are the corresponding maximum stresses associated with each direction, $t_{sh}^0 = \sqrt{(t_1^0)^2 + (t_2^0)^2}$ is the resultant shear stress. The corresponding separations are denoted by $\delta_i (i = 1,2,3)$, where the resultant planar shear separation is defined by $\delta_{sh}^0 = \sqrt{(\delta_1^0)^2 + (\delta_2^0)^2}$ and $\delta_3 = \delta_{norm}$ is the normal separation of the cohesive surfaces. Delamination was propagated using a mixed-mode relationship proposed by Benzeggagh and Kenane (B-K propagation criterion) [35],

$$G_c = G_{Ic} + (G_{IIc} - G_{Ic})\mathrm{B}^{\eta}, \tag{15}$$

where G_c is the mixed-mode fracture toughness, B is the local mixed-mode ratio defined as $B = G_{shear}/(G_I + G_{shear})$ and η is the mixed-mode interaction. The mixed-mode softening law is shown in Fig. 10.

4.3 Model definition

Models of the corrugated specimens were created in ABAQUS/Explicit 6.12, as shown in Fig. 11a. The geometry was meshed using an approximate element size of 0.5mm in the longitudinal (crush direction) and 1mm in the transverse directions. In order for C3D8R elements to capture the bending behaviour, three elements through the thickness of each ply were used. To suppress spurious energy

modes, an enhanced stiffness-based hourglass and distortion control were employed. The surface based cohesive behaviour was employed to capture delamination between adjacent plies. A general contact algorithm was utilised to generate a contact force between contact surfaces. 'Hard' contact conditions were defined between the platen and the plies as well as adjacent plies. The platen was modelled as an analytical rigid surface. The friction coefficients of ply-to-ply and ply-to-metal contact were set to 0.28 and 0.2 respectively, measured in [36]. The computational loading speed was fixed at 1m/s to reduce the CPU time whilst ensuring that the quality of the results was not affected by inertial effects. Selective mass scaling, which only scaled elements whose stable time increment was below 5e-08 s, was also employed during the crushing process to achieve a reasonable run time. Low-pass filters were employed to remove the numerical oscillations which are an artefact of explicit dynamic modelling. Models were run on a Windows Cluster with 16 CPUs with a run time of between 32 and 40 hours, depending on the specimen type.

4.4 Element deletion strategy

An efficient strategy to delete distorted element is to track the value of the determinant of the deformation gradient ($\det \mathbf{F}$) which is available directly from ABAQUS. $\mathrm{Det}\ \mathbf{F}$ yields the ratio of the deformed volume, *V*, to the undeformed, V_0, volume of an element, $\det \mathbf{F} = V/V_0$. The overall element distortion criterion was subsequently based on both the fibre-dominated longitudinal damage parameter, $d_{11}^{T(C)}$, and limits on $\det \mathbf{F}$ for tracking large changes in element volume,

$$\text{Delete element if} \begin{cases} d_{11}^{T(C)} > 0.99 \\ 0 < \det \mathbf{F} < 0.8 \; or \; \det \mathbf{F} > 1.2 \end{cases} \tag{16}$$

The limits on $\det \mathbf{F}$ are user-defined and the quoted values were found to yield reliable results. Further discussion on the choice of these limits is given in Section 5.5.

4.5 Material properties

Basic mechanical properties such as elastic stiffness, Poisson ratio and strength for AS4/PEKK were obtained from published data [37]. Double-cantilever-beam (DCB) [38], four-point end-notched flexure (4ENF) [39] and Mixed-mode bending (MMB) [40] tests were used to determine initiation/propagation interlaminar fracture toughness in mode I, mode II and mixed-mode, respectively. Compact Tension (CT) and Compact Compression (CC) tests [41, 42] were employed to measure the longitudinal tensile and compressive intralaminar fracture toughness. V-notched rail shear tests were employed to measure the non-linear behaviour and fracture toughness associated with shear loading [43]. The measured values from [20] given in Table 1 were then used as input material parameters to model the crushing behaviour.

5. Results and discussion

The experimental force-displacement curves show similar behaviour with some oscillatory noise particularly in the plateau phase where steady-state crushing occurs. DIC tests were performed to investigate the out-of-plane movement and strain value during crushing. The out-of-plane displacements of the undamaged parts of the specimens were negligible (Fig. 11b), proving that no buckling or out-of-plane movement occurred during crushing.

5.1 Overall response

At the beginning of the crushing process (cf. stage 1, Fig 12a, Fig 14a), damage was primarily in the form of local fragmentation as the trigger region was consumed. The reaction force increased gradually to the peak load at which point the entire uniform cross-section of the crush element came in contact with the platen. For all specimens, the peak load occurred at a displacement of S=2.4mm~2.7mm. At stage 2, delamination initiated with a splaying mode accompanied by extensive fibre tensile and compressive fracture in the high-curvature area (highlighted in stage 2 of

Fig. 13b and Fig. 15b), leading to a sudden drop in the reaction force as the chamfer is consumed. From stage 3 to stage 6, outer plies deform by bending (refer to the region to the left of the specimen edge, in Fig. 14c and Fig. 14c) and the inner plies tend to undergo crushing (refer to the region to the right of the specimen edge, in Fig. 14c and Fig. 14c). Internal debris was also created and acted like a 'wedge' in driving delamination. A typical mode I delamination was driven by the debris wedge in the Hat-3p specimen of Fig. 6b.

The numerical results in Fig. 14a and Fig. 12a achieved excellent quantitative correlation with experimental data without the need of calibrating any of the carefully obtained input data [20]. The initial stiffness, peak force (F_P) and steady-state force (F_{SS}) were predicted by the numerical model with good accuracy. The sudden load drop after the peak force is attributed to fibre fracture (element deletion in the numerical simulation) and extensive delamination after the chamfer trigger was fully consumed. The progressive nature of the crushing was well captured, with a clear plateau during the steady state crushing. The overall numerical oscillations are the result of element deletion laws invoked as part of the solution and artefacts of the explicit dynamic simulation.

5.2 Crushing morphology

The numerical results from Fig. 13 and Fig. 15 showing the crushing morphology confirm the qualitative accuracy of the present damage model. Matrix cracking, shear fracture, delamination, lamina bending and fragmentation were well predicted. The virtual formation of fronds around the circumference shows excellent qualitative similarity when compared with experimental results.

5.3 Energy dissipated mechanisms

The evolution of energy dissipated through various mechanisms during crushing is illustrated in Fig. 12 and Fig. 14 for the Semi-3p and Hat-3p specimens, verifying the energy balance relationship between external work done and energy absorbed. The predicted total dissipated energy was in good agreement with the experimental total absorbed energy. The majority of energy was dissipated

through intralaminar damage combining fibre tensile /compressive damage (e.g. 34.4% in the Semi-3p specimen) and matrix tensile/compression/shear damage (e.g 23.5% in the Semi-3p specimen), followed by the friction between the crushing platen and specimen and internal friction between the plies (e.g.15.1% in the Semi-3p specimen). Extensive delamination (green line) contributed 12.8% (in Semi-3p) of the total energy dissipation. The small amount of viscous energy dissipated is due to the use of the bulk viscosity method to damp out spurious oscillations in explicit dynamic simulations.

5.4 Crashworthiness assessment

The average crashworthiness performance results for different types of corrugated structures are presented in Table 2. The Semi-3p specimen has an SEA of 110.12 kJ/kg which may be compared to an identical specimen made from carbon fibre (CF)/epoxy and tested by Feraboli [5], where the SEA was reported as 70 kJ/kg for standard epoxy and 93 kJ/kg for toughened epoxy. The SEA of AS4/PEKK shows an increase of 57.3% and 18.4% respectively, indicating the significant energy absorption, and consequently crashworthiness performance improvement, of thermoplastic composite structures compared to their thermoset counterparts. This is primarily due to the superior fracture toughness of the thermoplastic matrix compared to thermoset matrix materials [44]. A comparison of SEA and crush efficiency between experimental and numerical results, in Fig. 16, confirms the predictive capability of the developed computational tool.

5.5 Sensitivity study of element deletion parameters

A sensitivity study of the element deletion conditions, based on $\det \mathbf{F}$, was conducted. Fig. 17a shows that increasing the upper limit of $\det \mathbf{F}$ (from the reference value of 1.2 to 1.4 and 1.6) doesn't affect the initial elastic region and peak load, but has some influence on the steady-state response. A

higher $\det \mathbf{F}$ limit results in an initially higher stead-state force, more load oscillations and subsequent lower steady-state force towards the end of the crush process but the overall energy dissipation is similar. It should be noted that the overall load responses for the following limits; (0.8-1.4) and (0.8-1.6) are still acceptable compared to the reference value (0.8-1.2) and experimental results.

Fig. 17b shows that with a lower limit of $\det \mathbf{F}$, i.e. 0.6 as opposed to 0.8, deletion of distorted elements is not activated. The higher level of element distortion leads to the solution aborting prematurely at an end-displacement of 15 mm. The lower limit representing the shrinkage of a volumetric element is very important in the crushing simulation as the dominated failure mode is compression. Element deletion is still eventually triggered by the upper limit of 1.2, shown in the Fig. 17b, but higher limits than this, combined with a limit lower than 0.8 lead to the solution aborting.

In the Fig. 17c, the crushing morphologies using different $\det \mathbf{F}$ limits are shown. The matrix damage results and element deletion areas are all very similar except for the cases of (0.6-1.4) and (0.6-1.6). For the last two cases, only delamination between plies was observed and no elements were deleted, which finally lead to highly distorted elements and the solution aborting.

These results indicate that a reasonable range of $\det \mathrm{F}$ may be used to capture the steady-state response during crushing. The current damage model accounts for different damage modes and there are often instances when considerable matrix damage has been accumulated but fibre-dominated damage has yet to be activated. This would imply that an element may still be able to support subsequent loading and deleting an element on the basis of accumulated damage in one mode may be premature, reducing the accuracy of the simulation. On the other hand, the failure in one mode may result in a high level of element distortion which may lead to the solution aborting. Increasing the robustness of the solution process involves balancing these two considerations. The

selected limits on $\det \mathbf{F}$ (0.8-1.2) were found to yield good results. This sensitivity study also confirmed that the sudden load drop following the initial peak load, in the load-displacement curve, was due to element deletion**.**

6. Conclusions

A detailed experimental and numerical investigation has been presented to validate the capability of a finite element-based damage model in predicting the energy absorption and consequently, the crashworthiness, of composite structures. Corrugated-shaped specimens, made from thermoplastic composites were manufactured and tested under quasi-static crushing loads. Excellent qualitative and quantitative correlation was achieved between the numerical models and experimental results. The fidelity of the computational models was able to provide detailed information on the evolution and propagation of splaying and fragmentation of the crushing composite, involving a complex interplay of fibre fracture, matrix cracking and delamination. The predictive capability of the numerical model enabled the relatively small difference between the responses of two specimen types, with slightly different cross-sectional geometries, to be captured and validated experimentally. For example, the specimens with semi-circular corrugations (Semi-3p) exhibited a slightly higher SEA than those with a 'hat' shaped cross-section (Hat-3p). The Semi-3p specimens where also compared to identically-shaped specimens made from thermoset composites and exhibited a 57.3% higher specific energy absorption compared to a standard CF/Epoxy specimen and 18.4% higher than CF/toughened epoxy specimens. Future work will focus on extending this computational damage model to capture strain rate effects which will enable accurate assessments of crashworthiness of composite structures in high energy crash events.

Acknowledgement

The corresponding author would like to acknowledge the financial support of Bombardier and the Royal Academy of Engineering. The authors would also like to gratefully acknowledge the funding from the Queen's University Belfast/China Scholarship Council (QUB/CSC) PhD Scholarship and the support from the Research Computing Team at QUB in accessing the HPC facilities. The authors would also like to gratefully acknowledge Mr Haibao Liu for helping with the mould design and specimen preparation.

References

[1] Vodicka R. Thermoplastics for Airframe Applications-A Review of the Properties and Repair Methods for Thermoplastic Composites. DSTO Aeronautical and Maritime Research Laboratory. 2006.
[2] Zarei H, Kro¨ger M, Albertsen H. An experimental and numerical crashworthiness investigation of thermoplastic composite crash boxes. Composite Structures. 2008;85(3):245-257.
[3] Waimer M, Kohlgrüber D, Hachenberg D, Voggenreiter H. Experimental study of CFRP components subjected to dynamic crash loads. Composite Structures. 2013;105:288-299.
[4] Heimbs S, Strobl F, Middendorf P. Integration of a composite crash absorber in aircraft fuselage vertical struts. International Journal of Vehicle Structures & Systems. 2011;3(2).
[5] Feraboli P. Development of a corrugated test specimen for composite materials energy absorption. J Compos Mater. 2008;42(3):229-256.
[6] Grauers L, Olsson R, Gutkin R. Energy absorption and damage mechanisms in progressive crushing of corrugated NCF laminates: Fractographic analysis. Compos Struct. 2014;110(0):110-117.
[7] Feraboli P, Wade B, Deleo F, Rassaian M, Higgins M, Byar A. LS-DYNA MAT54 modeling of the axial crushing of a composite tape sinusoidal specimen. Composites Part A: Applied Science and Manufacturing. 2011;42(11):1809-1825.
[8] David M, Johnson AF. Effect of strain rate on the failure mechanisms and energy absorption in polymer composite elements under axial loading. Composite Structures. 2015;122:430-439.
[9] Johnson AF, David M. Failure mechanisms in energy-absorbing composite structures. Philosophical Magazine. 2010;90(31-32):4245-4261.
[10] SIMULIA U. Simulating composites crush and crash events using ABAQUS. 50th AIAA/ASME/ASCE/AHS/ASC Structures, Structural Dynamics, and Materials Conference. 2009.
[11] Pinho S, Camanho P, De Moura M. Numerical simulation of the crushing process of composite materials. Int J Crash. 2004;9(3):263-276.
[12] Palanivelu S, Van Paepegem W, Degrieck J, Kakogiannis D, Van Ackeren J, Van Hemelrijck D, et al. Parametric study of crushing parameters and failure patterns of pultruded composite tubes using cohesive elements and seam, Part I: Central delamination and triggering modelling. Polym Test 2010;29(6):729-741.
[13] Fleming DC. Modelling composite crushing initiation using a cohesive element formulation. Int J Crash. 2011;16(5):475-485.
[14] Sokolinsky VS, Indermuehle KC, Hurtado JA. Numerical simulation of the crushing process of a corrugated composite plate. Composites Part A. 2011;42(9):1119-1126.
[15] Falzon BG, Apruzzese P. Numerical analysis of intralaminar failure mechanisms in composite structures. Part II: Applications. Compos Struct. 2011;93(2):1047-1053.
[16] Falzon BG, Apruzzese P. Numerical analysis of intralaminar failure mechanisms in composite structures. Part I: FE implementation. Compos Struct. 2011;93(2):1039-1046.
[17] Faggiani A, Falzon BG. Predicting low-velocity impact damage on a stiffened composite panel. Composites Part A: Applied Science and Manufacturing. 2010;41(6):737-749.
[18] Tan W, Falzon BG, Chiu LNS, Price M. Predicting low velocity impact damage and Compression-After-Impact (CAI) behaviour of composite laminates. Composites Part A: Applied Science and Manufacturing. 2015;71:212-226.

[19] Tan W, Falzon BG, Price M. Predicting the crushing behaviour of composite material using high-fidelity finite element modelling. International Journal of Crashworthiness. 2015;20(1):60-77.
[20] Tan W., Falzon BG, Price, M, Liu, H. The role of material characterisation in the crush modelling of thermoplastic composite structures. 2016; http://dx.doi.org/10.1016/j.compstruct.2016.07.011
[21] Israr HA, Rivallant S, Bouvet C, Barrau JJ. Finite element simulation of 0°/90° CFRP laminated plates subjected to crushing using a free-face-crushing concept. Composites Part A: Applied Science and Manufacturing. 2014;62:16-25.
[22] Grauers L, Olsson R, Gutkin R. Energy absorption and damage mechanisms in progressive crushing of corrugated NCF laminates: Fractographic analysis. Compos Struct. 2014;110:110-117.
[23] Palanivelu S, Paepegem WV, Degrieck J, Vantomme J, Kakogiannis D, Ackeren JV, et al. Crushing and energy absorption performance of different geometrical shapes of small-scale glass/polyester composite tubes under quasi-static loading conditions. Composite Structures. 2011;93(2):992-1007.
[24] Chiu LNS, Falzon BG, Ruan D, Xu S, Thomson RS, Chen B, et al. Crush responses of composite cylinder under quasi-static and dynamic loading. Composite Structures. 2015;131:90-98.
[25] Lemaitre J, Chaboche J-L. Mechanics of solid materials: Cambridge university press; 1994.
[26] Van Paepegem W, De Baere I, Degrieck J. Modelling the nonlinear shear stress–strain response of glass fibre-reinforced composites. Part II: Model development and finite element simulations. Composites Science and Technology. 2006;66(10):1465-1478.
[27] Van Paepegem W, De Baere I, Degrieck J. Modelling the nonlinear shear stress–strain response of glass fibre-reinforced composites. Part I: Experimental results. Composites Science and Technology. 2006;66(10):1455-1464.
[28] Vogler M, Rolfes R, Camanho P. Modeling the inelastic deformation and fracture of polymer composites–Part I: plasticity model. Mechanics of Materials. 2013;59:50-64.
[29] Camanho P, Bessa M, Catalanotti G, Vogler M, Rolfes R. Modeling the inelastic deformation and fracture of polymer composites–Part II: smeared crack model. Mechanics of Materials. 2013;59:36-49.
[30] Vyas GM, Pinho ST, Robinson P. Constitutive modelling of fibre-reinforced composites with unidirectional plies using a plasticity-based approach. Composites Science and Technology. 2011;71(8):1068-1074.
[31] Puck A, Schürmann H. Failure analysis of FRP laminates by means of physically based phenomenological models. Compos Sci Technol. 1998;58(7):1045-1067.
[32] Catalanotti G, Camanho PP, Marques AT. Three-dimensional failure criteria for fiber-reinforced laminates. Composite Structures. 2013;95:63-79.
[33] Press WH. Numerical recipes in Fortran 77: the art of scientific computing: Cambridge university press; 1992.
[34] Simulia. Abaqus 6.12 documentation. Providence, Rhode Island, US. 2012.
[35] Benzeggagh M, Kenane M. Measurement of mixed-mode delamination fracture toughness of unidirectional glass/epoxy composites with mixed-mode bending apparatus. Composites Science and Technology. 1996;56(4):439-449.
[36] Tan W, Falzon BG. Modelling the nonlinear behaviour and fracture process of AS4/PEKK thermoplastic composite under shear loading. Composites Science and Technology. 2016;126:60-77.
[37] Cytec. APC-2 PEKK Thermoplastic Polymer Technical Data Sheet. Cytec Engineering Materials. 2012.
[38] ASTM. Standard Test Method for Mode I Interlaminar Fracture Toughness of Unidirectional Fiber-Reinforced Polymer Matrix Composites. D5528-13, West Conshohocken, PA 2013.
[39] Offringa A, List J, Teunissen J, Wiersma H. Fiber reinforced thermoplastic butt joint development. Proceedings of International SAMPE Symposium and Exhibition, 2008.
[40] ASTM. Mixed Mode I-Mode II Interlaminar Fracture Toughness of Unidirectional Fibre Reinforced Polymer Matrix Composites. D6671/D6671M-13e1, West Conshohocken, PA2013.
[41] Jose S, Ramesh Kumar R, Jana M, Venkateswara Rao G. Intralaminar fracture toughness of a cross-ply laminate and its constituent sub-laminates. Composites Science and Technology. 2001;61(8):1115-1122.
[42] Pinho ST, Robinson P, Iannucci L. Fracture toughness of the tensile and compressive fibre failure modes in laminated composites. Composites Science and Technology. 2006;66(13):2069-2079.
[43] ASTM. Standard Test Method for Shear Properties of Composite Materials by V-Notched Rail Shear Method. D7078/D7078M-12, West Conshohocken, PA2012.
[44] Jacob GC, Fellers JF, Simunovic S, Starbuck JM. Energy absorption in polymer composites for automotive crashworthiness. J Compos Mater. 2002;36(7):813-850.
[45] Dao M, Asaro RJ. On the critical conditions of kink band formation in fiber composites with ductile matrix. Scripta materialia. 1996;34(11):1771-1777.

Figures

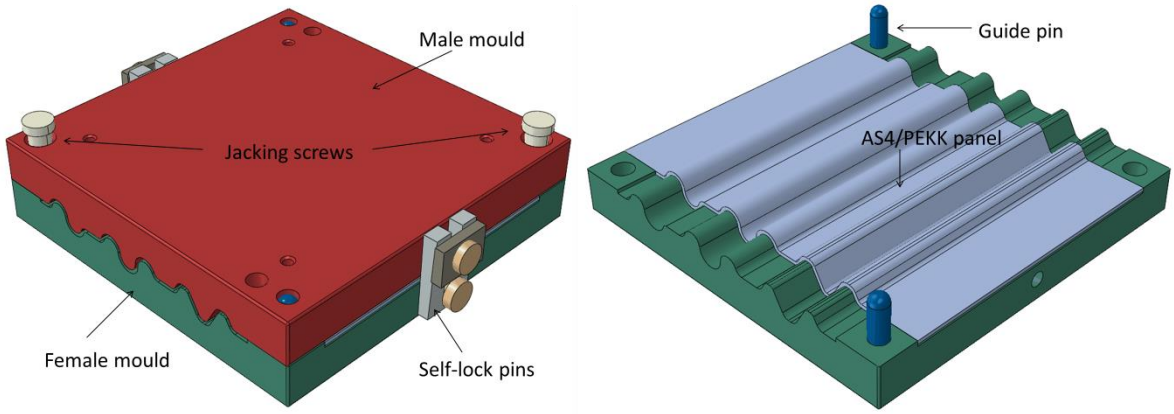

Fig. 1. Moulding tool for the manufacture of AS4/PEKK corrugated panels.

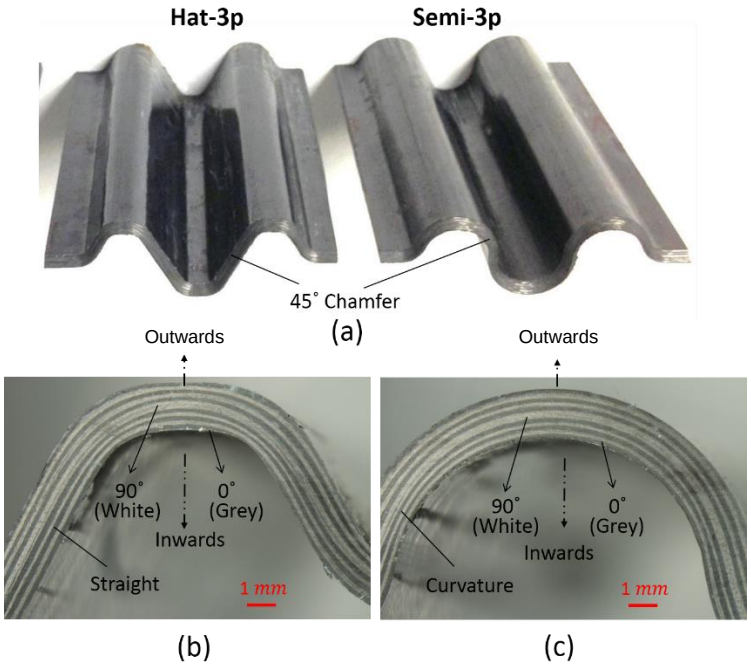

Fig. 2. (a) Test specimens with chamfer triggers; Optical microscopy of cross-section of (b) hat specimen and (c) semi-circular specimen.

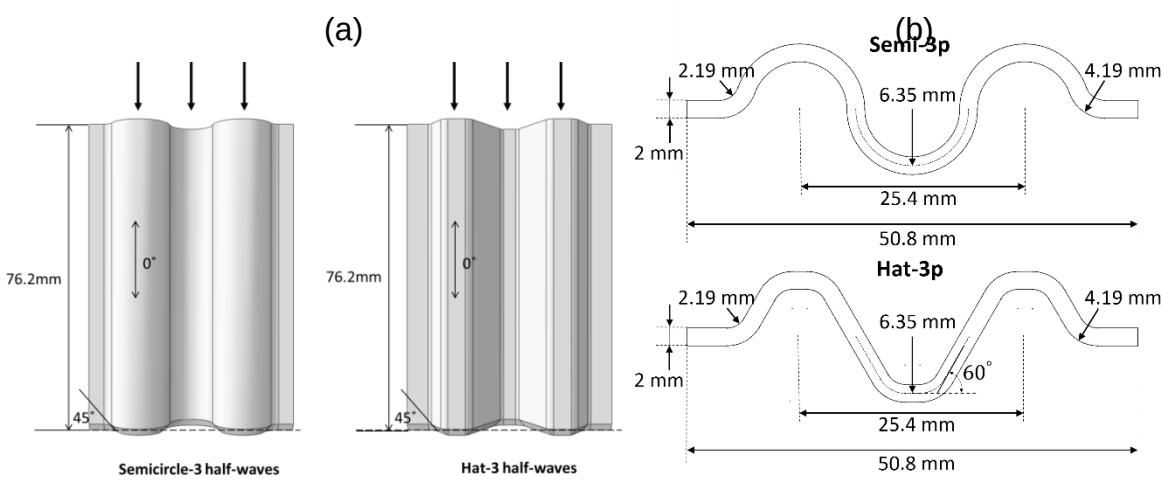

Fig. 3. Specimen geometries produced from each manufactured panel (a) chamfer and loading direction and (b) cross-section dimensions (mm).

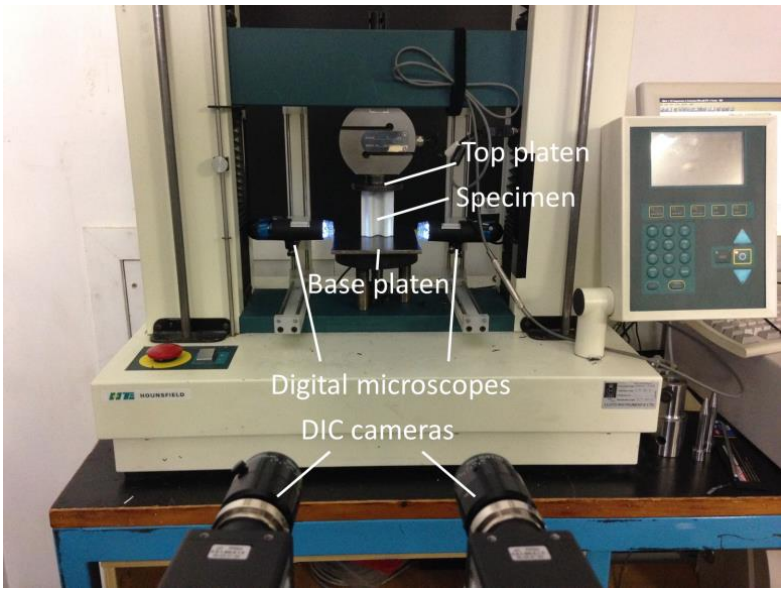

Fig. 4. Crushing test set-up with digital microscopes and DIC cameras.

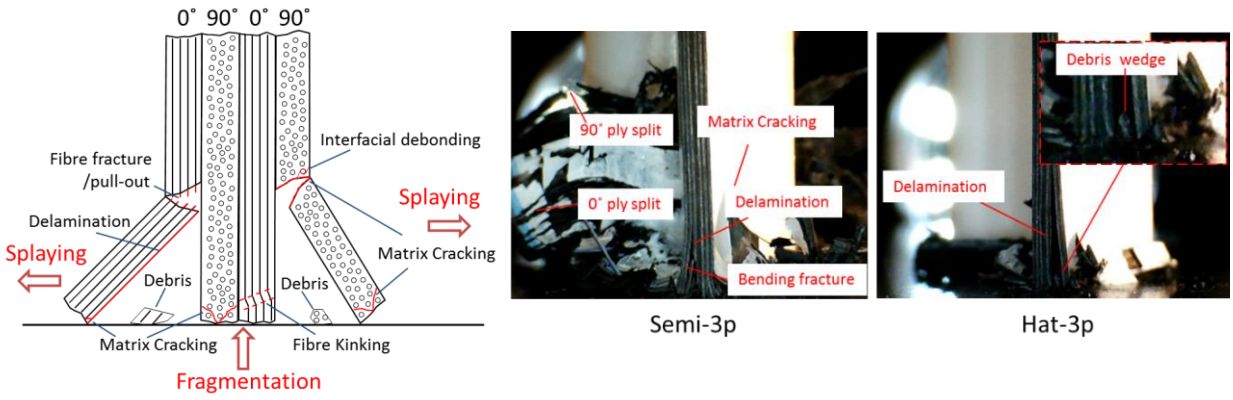

Fig. 5. Axial direction: (a) damage mechanisms in 90˚ and 0˚ plies (b) side view of crush tests on two specimen types.

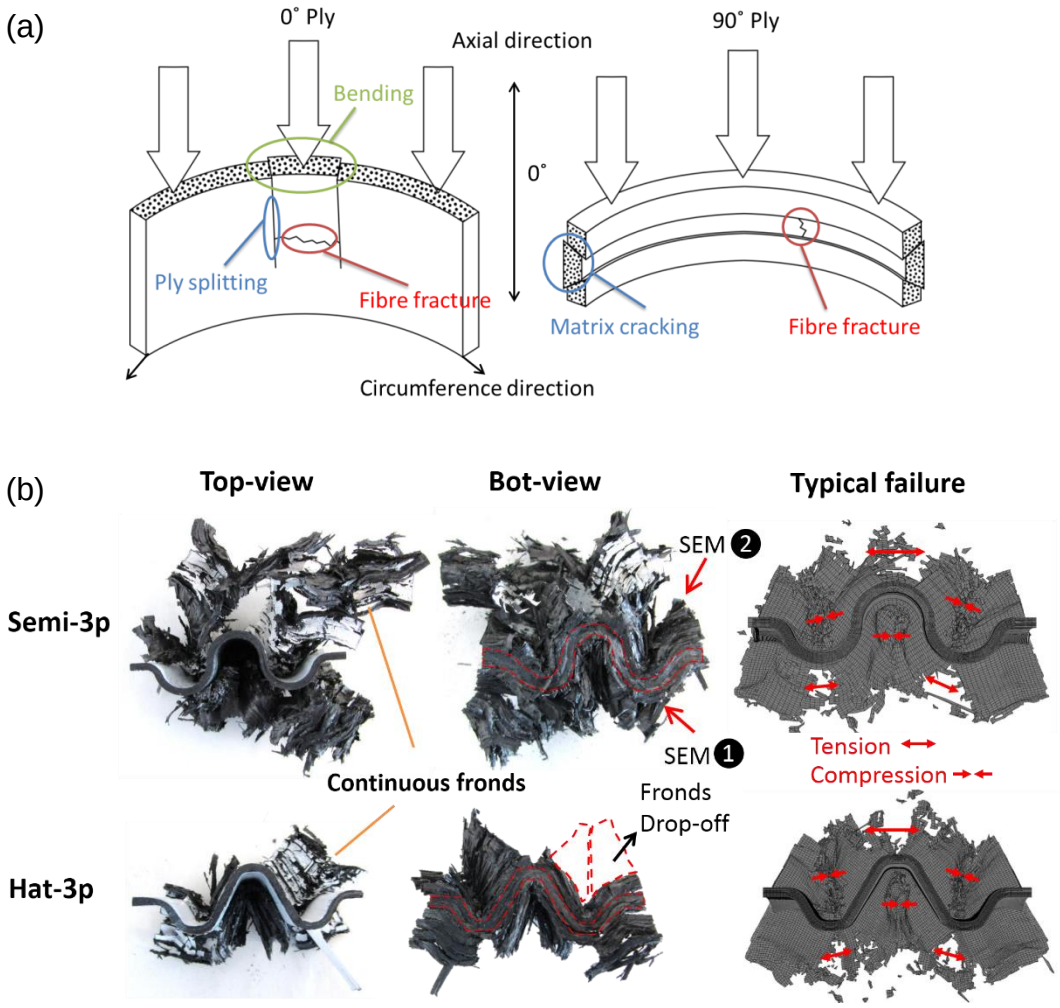

Fig. 6. Circumferencial direction: Typical damage mechanisms (a) damage mechanisms in 0˚ and 90˚ plies (b) typical failure morphologies of tested specimens.

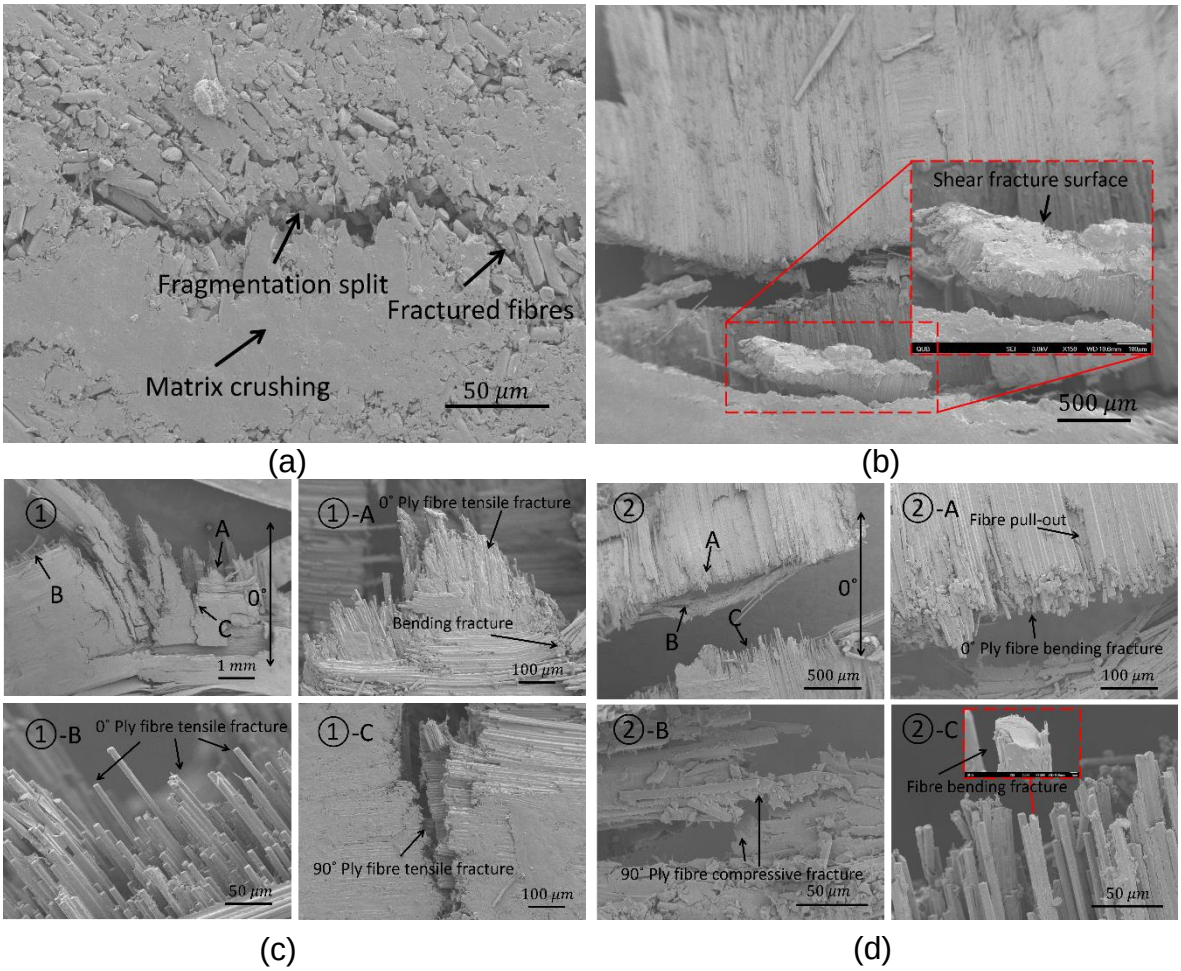

Fig. 7. SEM images (a) crushed surface (b) typical shear fracture (c) failure mode in the outwards part (d) failure mode in the inwards part.

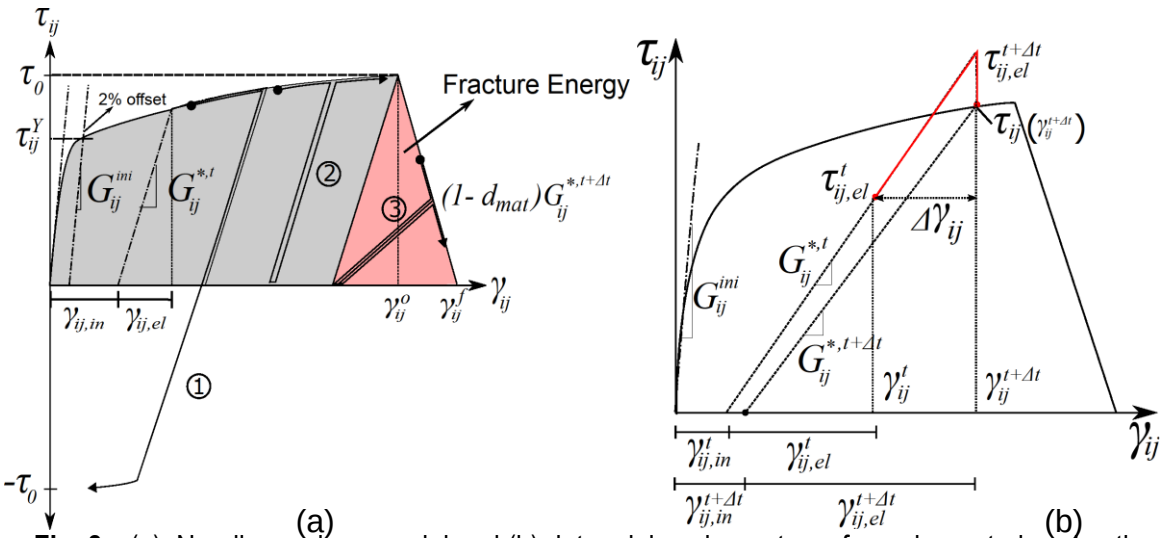

Fig. 8. (a) Non-linear shear model and (b) determining shear stress from shear strain using the

elastic predictor method

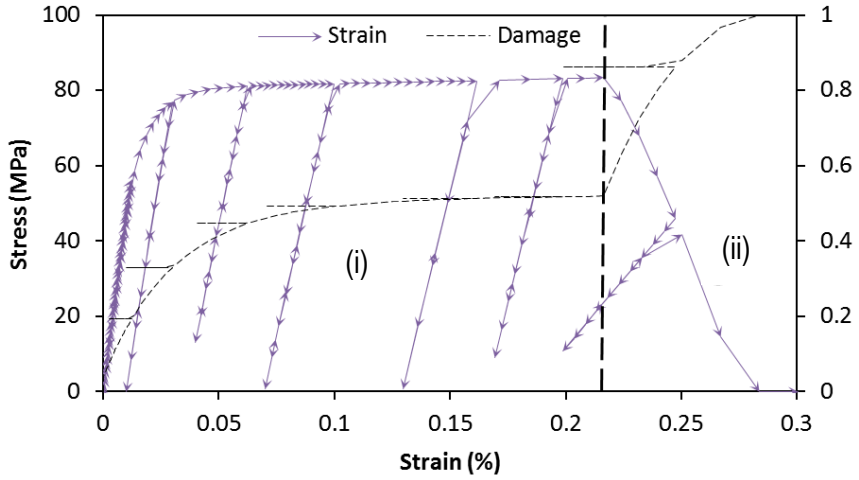

Fig. 9. Stress-strain constitutive law for non-linear shear

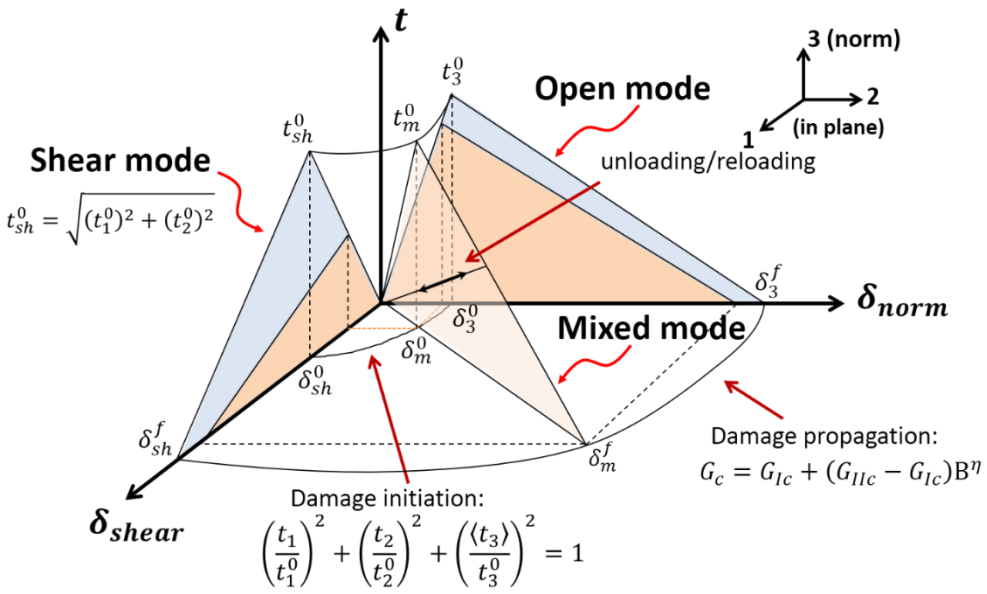

Fig. 10. Mixed-mode softening law of cohesive zone model.

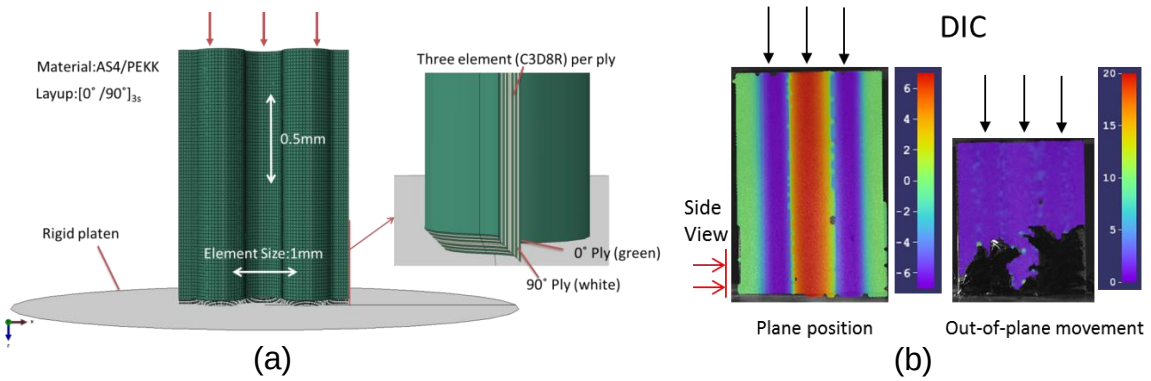

Fig. 11. (a) Finite element model of Semi-3p specimen (b) DIC results

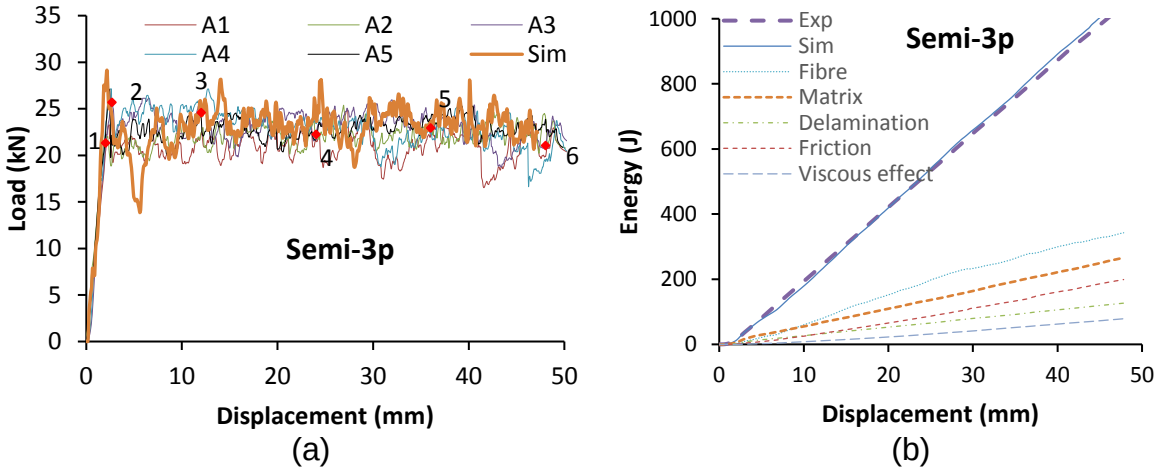

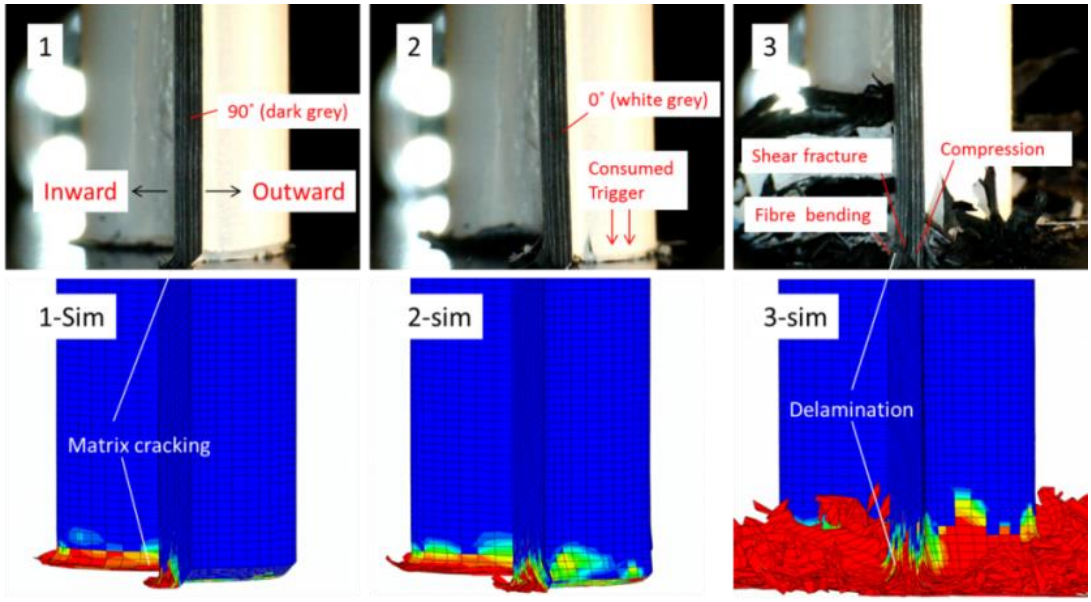

Fig. 12. Semi-3p specimen: (a) load-displacement curves (b) energy dissipation mechanisms of Semi-3p specimen (c) side view of the failure process.

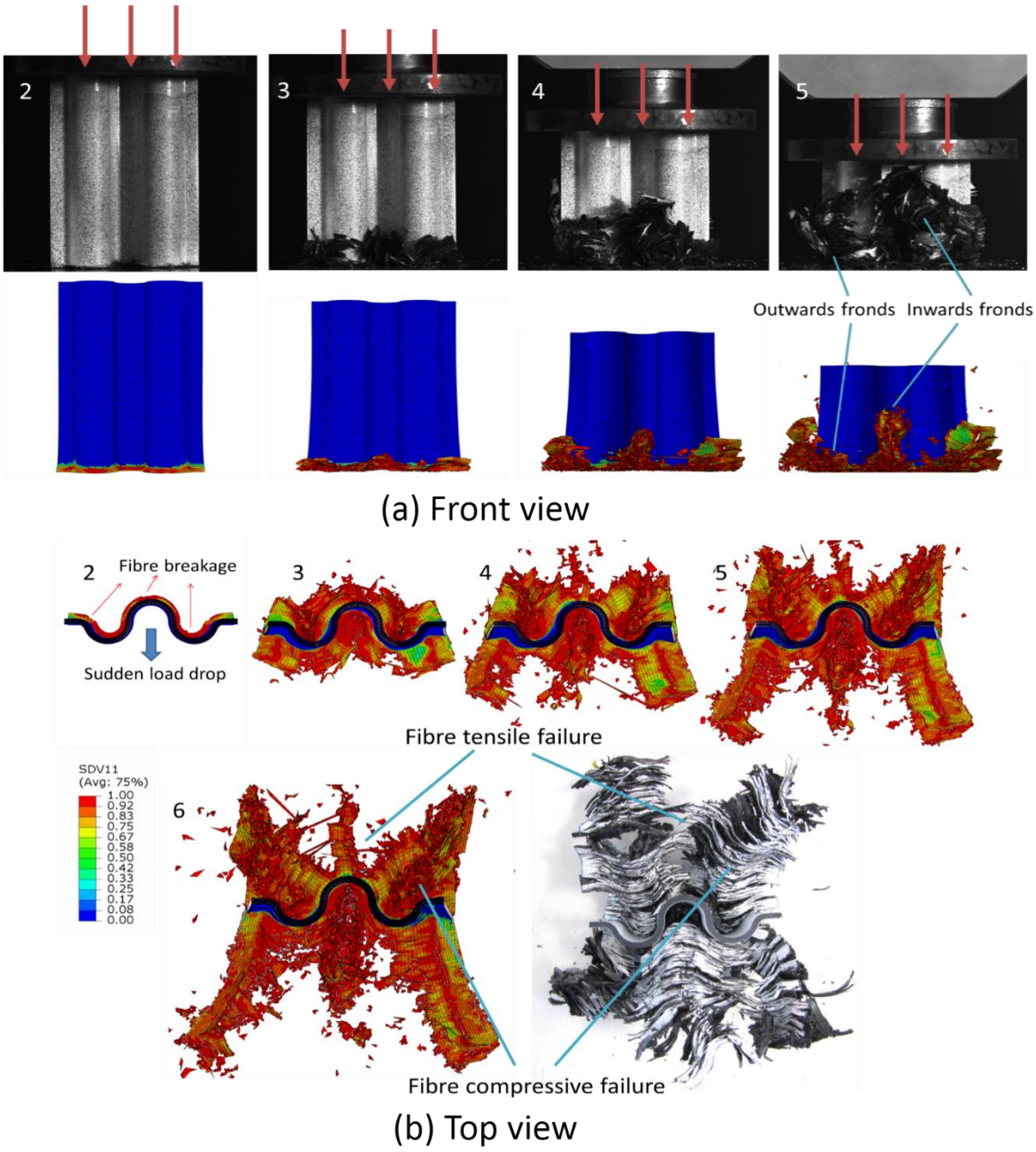

Fig. 13. Semi-3p specimen: experimental crush morphology and numerical matrix damage results (a) front and (b) top view.

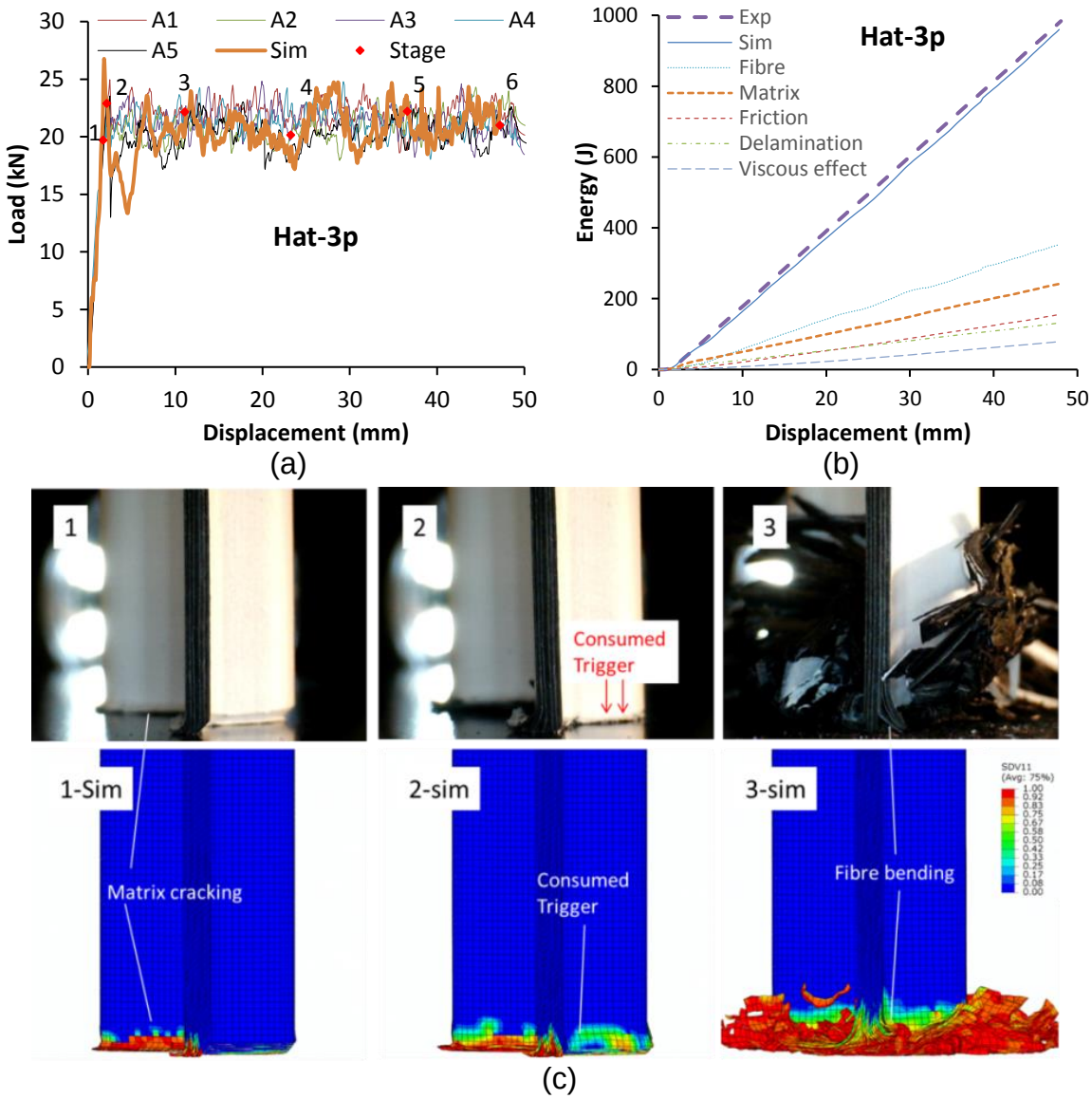

Fig. 14. Hat-3p specimen:(a) load-displacement curves (b) energy dissipation mechanisms of Hat-3p specimens (c) side view of the failure process.

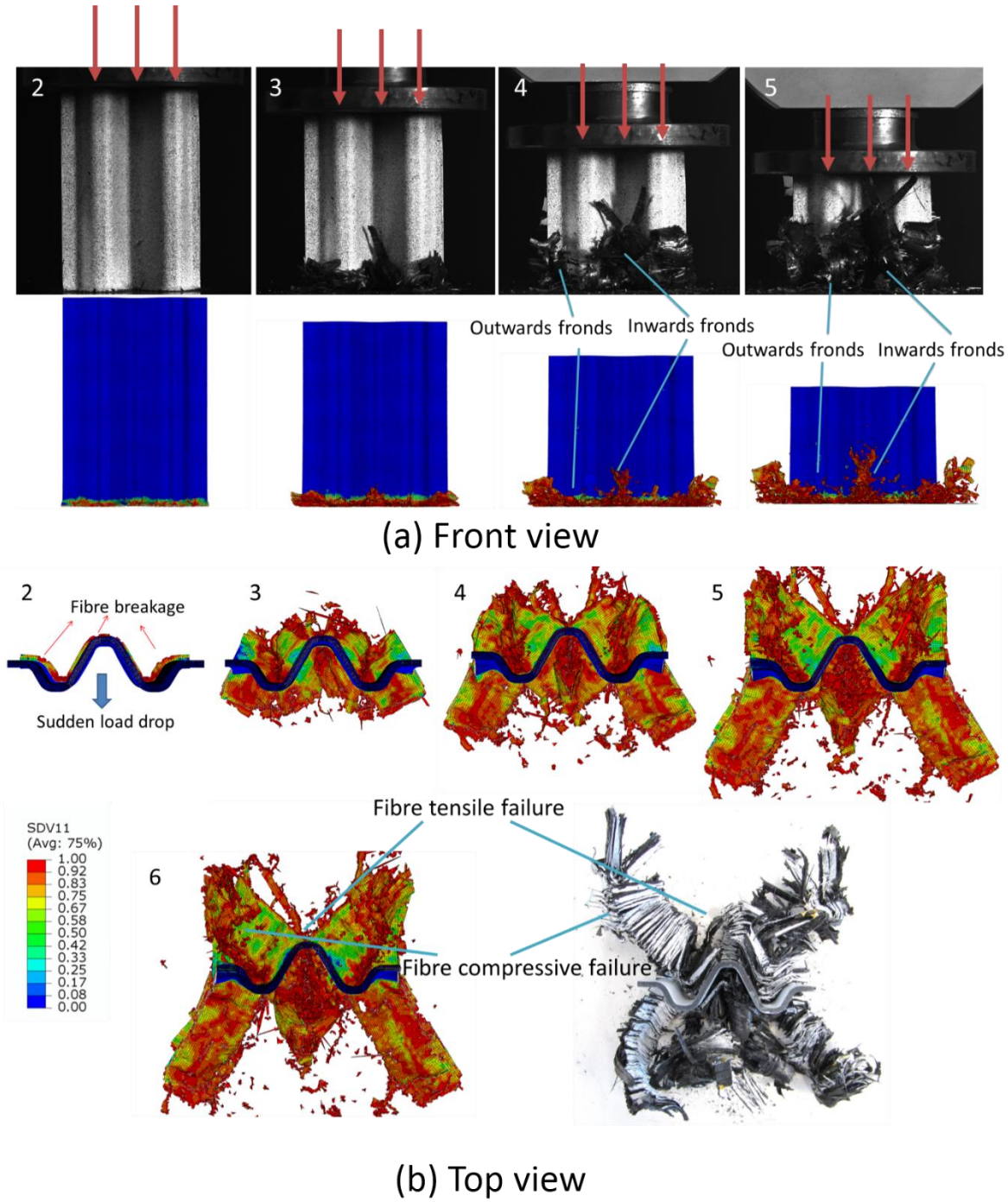

Fig. 15. Hat-3p specimen: experimental crush morphology and numerical matrix damage results (a) front and (b) top view.

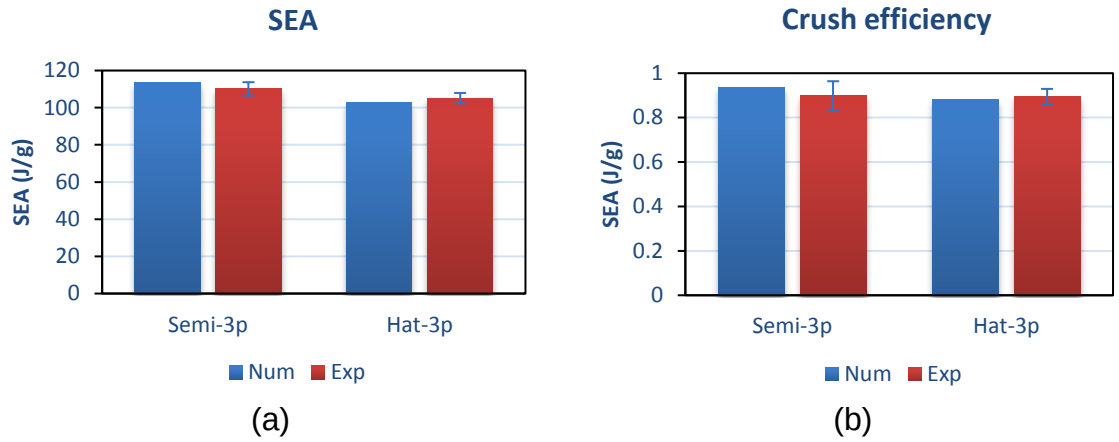

Fig. 16. Comparison of experimental and numerical results of (a) SEA and (b) crush efficiency.

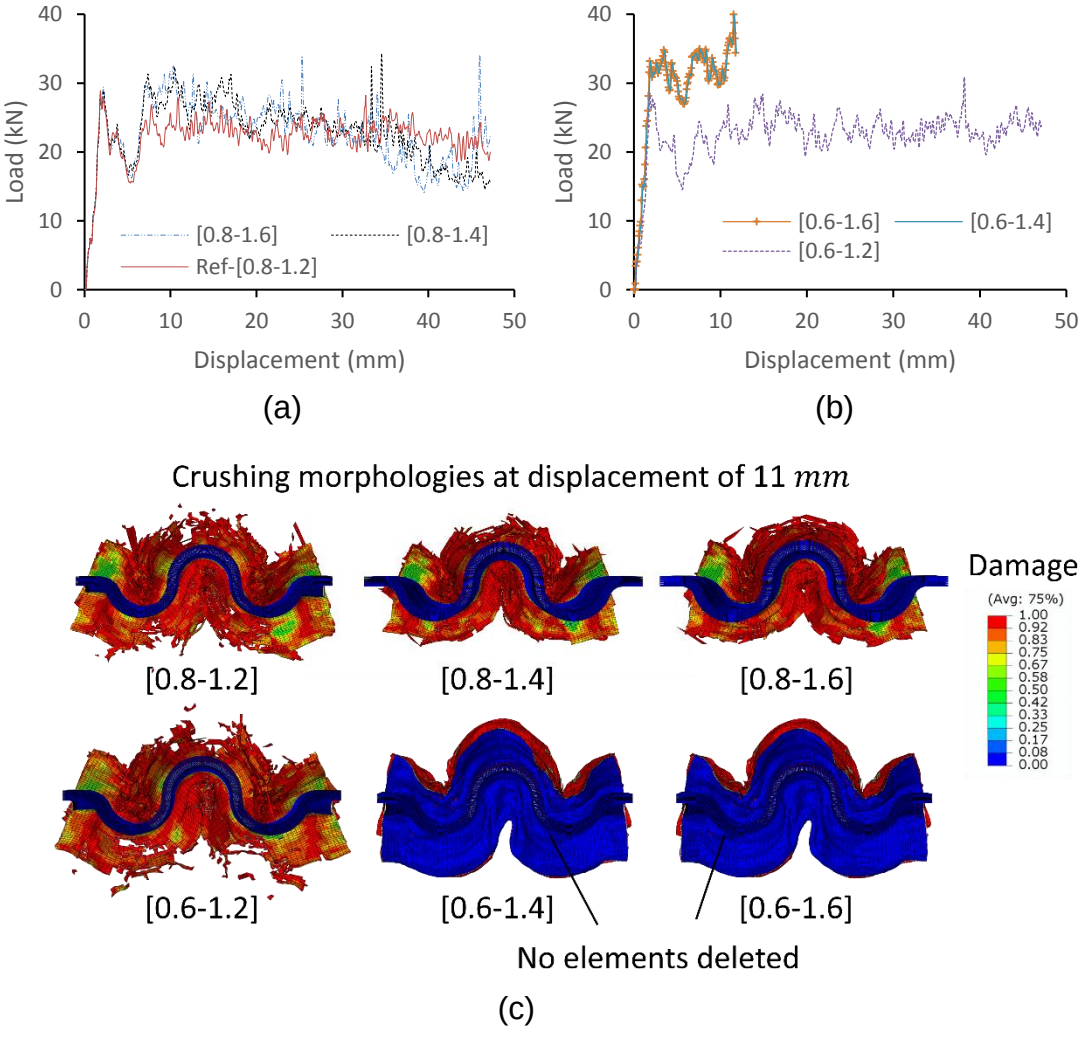

Fig. 17. Predicted load-displacement curves with (a) increased upper limit on $\det \boldsymbol{F}$ (b) decreased lower limit on $\det \boldsymbol{F}$ and (c) damage contours using different limits on $\det \boldsymbol{F}$.

Tables

Table 1. Material Properties of AS4/PEKK for numerical simulation

Property	Values
Elastic Properties [37, 45]	$\mathrm{E}_1 = 139GPa;\ \mathrm{E}_2 = \mathrm{E}_3 = 10.3GPa;\ \mathrm{G}_{23} = 3.96GPa;$ $\mathrm{G}_{12} = \mathrm{G}_{13} = 5.2GPa;\ \nu_{12} = \nu_{13} = 0.3;\ \nu_{23} = 0.3;$
Strength [37]	$X_T = 2463MPa;\ X_C = 1493MPa;\ Y_T = 102MPa;\ Y_C = 254MPa;\ \mathrm{S}_{12} = \mathrm{S}_{13} = 80.81MPa$
Intralaminar Fracture Toughness [20]	$\Gamma_{11}^{\mathrm{T}} = 243.9kJ/m^2;\ \Gamma_{11}^{\mathrm{C}} = 108.3kJ/m^2;\Gamma_{22}^{\mathrm{T}} = 1.564kJ/m^2;\Gamma_{22}^{\mathrm{C}} = 34.58kJ/m^2;\Gamma_{12} = \Gamma_{23} = \Gamma_{13} = 34.58kJ/m^2;$
Non-linear Shear Properties [20]	$\tau_{ij}^0 = 80.81;\ \alpha = 0.16;\ \beta = -44.26$ $\mathrm{p}_1 = 2405;\ \mathrm{p}_2 = -32.59;\ \mathrm{p}_3 = 2596;\ \mathrm{p}_4 = -0.1764$
Interface Properties [20]	$G_{IC} = 1.564kJ/m^2;\ G_{IIC} = 2.113kJ/m^2;\ \eta = 0.996;$ $\tau_3^0 = 61MPa;\ \tau_{1(2)}^0 = 68.4MPa;k = 1 \times 10^5 N/mm^3$

Table 2. Experimental results of crashworthiness performance (S.D.: Standard deviation)

	Semi-3p	**S.D.**	**Hat-3p**	**S.D.**
EA (kJ)	1090.22	39.26	1035.93	28.71
SEA (kJ/kg)	110.12	3.97	105.17	2.91
Peak force (kN)	25.05	2.04	23.64	0.92
Steady force (kN)	22.39	0.81	21.12	0.60
Mean crush stress (MPa)	175.74	6.39	167.54	4.78
CE (-)	0.90	0.06	0.89	0.03